COUPLED CFD-CSM ANALYSES OF A HIGHLY FLEXIBLE TRANSPORT AIRCRAFT BY MEANS OF GEOMETRICALLY NONLINEAR METHODS

Markus Zimmer[1], Johan M. Feldwisch[1], Markus Ritter[1]

[1]German Aerospace Center (DLR)
Bunsenstraße 10, 37073 Göttingen, Germany
Markus.Zimmer@dlr.de
Johan.Feldwisch@dlr.de
Markus.Ritter@dlr.de

Keywords: CFD, CSM, computational aeroelasticity, geometrically large deformations, non-linear loads analysis, very flexible aircraft

Abstract: The ever lasting race towards increased efficiency in the aircraft industry has resulted in excessively slender and light weight airframes. Utilising the anisotropic characteristics of specifically tailored composites is one key driver, enabling structural concepts which were impossible a few decades ago. The results are highly flexible aircraft structures, pushing geometrically linear methods to their limits. One example of such a concept is the Boeing 787 which reaches wing tip displacements of approximately 10 % of the wing half span already during cruise flight.

Thus, loads and flight dynamics analyses have to be developed which are accurate in the context of large deflections. By utilising a coupled CFD-CSM analysis in combination with a highly flexible long range jet transport model, this paper aims to establish the groundwork for a high fidelity geometrically nonlinear loads framework. In this publication, a general methodology to compute static manoeuvre cases with deflections of up to 25 % is presented. Furthermore, by computing rigid and elastic polars as well as calculating pull up and push down manoeuvres, the differences between geometrically linear and nonlinear simulations are illustrated with respect to aerodynamic parameters, cut loads, and strains.

NOMENCLATURE

Symbols

α	= angle of attack	$\boldsymbol{K}$	= stiffness matrix
ξ	= tolerance	l, m, n	= roll, pitch, yaw moment
b	= half span	$\boldsymbol{\Omega}$	= vector of angular velocities
C_D	= drag coefficient	$\boldsymbol{J}$	= inertia tensor
C_f	= skin friction coefficient	$\boldsymbol{L}$	= moment vector
C_L	= lift coefficient	$\boldsymbol{M}$	= mass matrix
c_{MA}	= mean aerodynamic chord	M	= Mach number
$\boldsymbol{F}$	= external load vector	m	= mass
$\boldsymbol{N}$	= internal element nodal forces	p, q, r	= roll, pitch, yaw rate
g	= acceleration due to gravity	q_0	= dynamic pressure
		r	= residual

$\boldsymbol{u}$	= displacement vector	f	= force
$\boldsymbol{v}$	= velocity vector	u	= displacement
V	= velocity	wt	= wing tip
x_0	= trim constraints	w	= wing
$\hat{y}$	= trim target states	**Abbreviations**	
$\tilde{n}$	= load factor	CFRP	= Carbon Fibre Reinforced Plastic
s	= force scaling factor		
t	= displacement scaling factor	FSDM	= Flow Simulator Data Manager
Sub- & Superscripts		HTP	= Horizontal Tailplane
1 - 6	= degrees of freedom	LRA	= Loads Reference Axis
b	= body reference frame	MTOM	= Maximum Take-Off Mass
i, k	= index	PAX	= Norm passenger

1 INTRODUCTION

Composite wing structures are already part of aircraft, as significant weight reductions are achieved. In the case of the Boeing 787, this leads to a more flexible wing structure, increasing the wing tip deformation during cruise to about 10 % with respect to the semi span. A potential benefit of such highly flexible wing structures is an increase in passenger comfort, e.g. during gust encounters and turbulence, and airframe stress reduction due to passive load alleviation. On the other hand, flexible wing structures may be caused by an increase in aspect ratio and a reduction in wing thickness as an attempt to boost aerodynamic performance. Deformations of 10 % and higher are considerably nonlinear. Therefore, for aeroelastic loads computations, the different combinations of linear and nonlinear simulation methods - aerodynamically and structurally - have to be assessed for highly flexible aircraft.

The presented work proposes analysis methods which incorporate effects caused by geometrically nonlinear wing deflections. As described by Ritter et al. in [1] the small displacement assumption of linear structural solvers in combination with a deformation of the aerodynamic model causes the lifting surface area to be stretched and increased, altering the lifting forces, moments balance, and trim state. As an extension to the work of Ritter, the proposed analyses utilises a comprehensive stiffened shell structure design of a long range jet transport.

Large deformations might also cause issues regarding the CFD-CSM coupling scheme, CFD volume deformation, force / displacement relaxation, and convergence of the structural solver. These potential obstacles need to be addressed in order to incorporate the loads in a robust structural optimisation process in the long term.

An example for such a framework is given by Grey et al. in [2], in which the authors depict a high fidelity optimisation routine using loads obtained from geometrically nonlinear analyses. Furthermore, the authors compare geom. linear and nonlinear structural analysis and conclude that linear analyses are not conservative with respect to loads. However, instead of a modern carbon fibre design, the authors employed isotropic materials. Moreover, this work lacks amount and diversity of load cases and neglects flight mechanical limits and certain structural constrains like buckling. The proposed method turns this procedure around, using a comprehensive linear framework to optimise the structure, while checking the result with high fidelity nonlinear methods at a later stage.

Consequently, for the present work, a highly flexible structure of a modern civil jet transport in the class of a Boeing 787 or an Airbus A350 is combined with high fidelity aerodynamics to conduct polar and trim simulations. Throughout this paper, the differences between rigid, geometrically linear, and nonlinear methods are analysed and compared for the changes in aerodynamic derivatives and structural failure indices. These analyses serve as the groundwork to a geometrically nonlinear loads framework.

2 SOFTWARE

The simulations of this work are based on several software packages and tools. For the geometric linear and nonlinear structural analysis the commercial software MSC.Nastran is used. The aerodyanmic forces are computed by the DLR TAU-Code, which has been developed at the DLR in the past decades. Furthermore, the FlowSimulator ecosystem provides multiprocessing capabilities for multiple data objects, which can be registered in a central data manager. Additionaly, multiple plugins for mesh manipulations are provided. Lastly, the MDA framework UltraFLoads is a high-level python layer which helps to orchestrate those tools in numerous types of analyses, e.g. static coupling, polar, manoeuvre, and more.

2.1 MSC.NASTRAN

MSC.Nastran is a commercial software system and offers a wide range of multidisciplinary analyses related to the finite element methods. In combination with a potential-flow based aerodynamic solver, aeroelastic problems like manoeuvers, divergence, control surface efficiency, flutter, and gust encounter can be analysed. Furthermore, multiple optimisation algorithms can be applied, to further improve a structural model, while considering responses and constraints from different types of analyses. Additionally, MSC.Nastran has been utilised for the calculation of loads and optimisation of the structural model. For this work, the SOL400 routine of MSC.Nastran V2021.1 is applied for which geometric linear and nonlinear analyses can be selected. In the context of nonlinear analyses, Nastran provides the updated Lagrangian method to solve large deflection problems, which is briefly described in Section 3.1.

2.2 TAU

The DLR TAU-Code is a highly validated CFD solver that uses hybrid, unstructured grids which allows to study the airflow about complex geometries. It has been developed over the past 25 years at the DLR Institute of Aerodynamics and Flow Technologies and has been applied in numerous academical and industrial projects. Further information about the DLR TAU-Code are provided by reference [3].

2.3 FlowSimulator

The FlowSimulator and DataManager (FSDM) has been jointly developed within the context of CFD simulations by Airbus, DLR and Onera in the past 15 years. It is an HPC library, which offers data-object like arrays, datasets, meshes for multiprocessing, and simplifies massively parallel simulations on compute clusters. Using a communication object, those data-objects can gather, distribute and broadcast information across processes. Furthermore, data-objects can be centrally registered in memory, reducing file-io and enabling software architectures with a centralised data model. An additional plugin layer adds for example mesh manipulation tools. The FSDM data-objects and the plugins are mainly written in C++ and made accessible to Python via Swig. On top, a control layer written in Python improves the convenient interaction with the FSDM data objects. With the central data registry and the different tools available in

the environment, researchers can define their own scenario scripts and execute them in a single Python session. The FSDM is described further in [4].

2.4 UltraFLoads

To further simplify the interaction with the FSDM, UltraFLoads, a Python tool developed at the DLR Institute of Aeroelasticity, offers pre-build scenarios as analysis. In UltraFLoads every scenario or simulation is seen as some sort of analysis. Hence, techniques like object oriented programming, abstract interfacing, and inheritance are applied. All analyses are are derived from one abstract base class. Down the inheritance tree, other abstraction layers are added to define interfaces for like structural analyses, aerodynamic analyses, or aero-structural analyses. Using interfaces for the different abstraction layers enables researchers to introduce own prototypes, without altering the source code.

A multidisciplinary analysis problem like aero-structural simulation works with the interface methods of the abstract aerodynamic analysis and abstract structure analysis. For example, a new structure prototype can be integrated easily by only implementing the abstract interface for structural analyses. As the centralized data model is a core idea of the FSDM, it is adopted by UltraFLoads. All inputs like parameters, settings, or monitoring are stored centrally and are accessed and modified by each analysis independently. As a consequence, data does not need to be passed from one analysis to another, which further simplifies decoupling of code.

As the framework is developed with focus on aeroelasticity, UltraFLoads additionally provides analysis for flight dynamics, trim, or aero-structural coupling. UltraFLoads has been applied to quasi-steady, rolling and pitching manoeuvers in [5] and showed very good agreement to flight test data of a steady turn manoeuvre of jet transoprt aircraft[6].

3 METHODOLOGY

The used analyses for this work are polar analyses and trim analyses. In the context of the polar analyses the structure is considered as rigid, geometrically linear or geometrically nonlinear. For the trim analyses, the rigid body acceleration needs to be determined and therefore, a flight mechanic analysis is used. The flight mechanic analyses works with the aero-structural analysis to evaluate the aerodynamic forces at the center of gravity. Following subsections describe the required analysis methods briefly.

3.1 Structural analysis

The finit element analysis is used in this work in order to calculate the static mechanical response to aerodynamic and inertia forces. This method uses the principal of continuum mechanics in order to discretise a structure by finite sub components for which the characteristics are described by analytical *shape functions*. By combining multiple elements, the global stiffness matrix K is assembled. For small rotations and displacements, simplifications and assumptions may be made in order to put the external forces vector F and the displacement vector u into a linear relation:

$$Ku = F. \tag{1}$$

However, for systems encountering large displacement and rotations, this simplifications are not valid, thus resulting in the stiffness matrix to be dependent on the displacements and the external loading. For some problems, even F may depend on u, resulting in *follower forces* which rotate based on the displacement field. This results in a nonlinear formulation of Eq. 1:

$$K(F, u)u = F(u). \tag{2}$$

4

This nonlinear correlation may not be easily solved by inverting $\boldsymbol{K}$. Instead an updated Largrange method is formulated by imposing an iterative Newton-Raphson-scheme. Consequently, the external load is divided into n steps. At each step i, the residual of the equilibrium condition is formulated by subtracting the internal element nodal forces and the external loads:

$$\boldsymbol{F}^i - \boldsymbol{N}^i = \boldsymbol{R}^i. \tag{3}$$

Using the definition of the tangential stiffness $\boldsymbol{K}_T$:

$$\boldsymbol{K}_T^i = -\frac{\partial \boldsymbol{R}^i}{\partial \boldsymbol{u}^i} \tag{4}$$

a linear equation system for the displacement increment $\Delta \boldsymbol{u}$ is formulated

$$\boldsymbol{K}_T^i \Delta \boldsymbol{u}^i = \boldsymbol{R}^{i-1} \tag{5}$$

and the new displacement field may be recovered using:

$$\Delta \boldsymbol{u}^i = \boldsymbol{u}^i - \boldsymbol{u}^{i-1}. \tag{6}$$

The presented work focuses on the aspect of tangential stiffness, in which the stiffness matrix is dependent on external loading and the displacement field. Follower forces are neglected in the context of the Lagrangian method. However, the deformation of the aerodynamic mesh based on the deflection of the structure, causes rotation of the force vectors perpendicular to the lifting surface on the outer aero-structural loop. For an in-depth description of the Lagrangian formulation it is referred to [7].

3.2 Aerodynamic analysis

The DLR-Tau code is used to calculate aerodynamic forces. In the context of this work, the steady RANS equations are solved using the negative Spalart-Allmaras (SA-Neg) turbulence model. The solver is started with a parameter set, in which an upwind scheme is selected for the inviscid flux discretisation. Once an initial solution is found, the inviscid flux discretisation is switched to a central scheme. Instead of prescribing the velocity boundary conditions at the far field, the grid velocities are defined by the motion (Euler angles, air speed, body rates). The computation of the grid velocities due to rigid body motion is then controlled by an external *motion module*. This approach is needed to define a pitch rate which is related to the load factor for a quasi-steady pull/push manoeuvre.

3.3 Volume Deformation

For the volume deformation a FlowSimulator plugin is used, which deformes the volumetric mesh based on radial basis methods. Flexible deformation groups are defined for several components of the surface patches, fixed groups in which the mesh is not supposed to be deformed, and no normal movement patches, in which nodes are not allowed to be displaced in the normal direction of a reconstructed plane. After each volume mesh deformation step, the mesh quality is analysed and cells with negative volumes are repaired by FlowSimulator plugins.

3.4 Aero-Structure analysis

As the aerodynamic forces depend on the elastic deformation, which again depends on the aerodynamic forces, the aero-structural problem is implicit and is solved in a loosely coupled iterative procedure as depicted in Algorithm 1.

Algorithm 1 The steady aero-structural analysis

Require: Aerodynamic analysis and Structural analysis

  function Execute

    $k = 1$

    $u_0 = 0$ **or** u_{Restart}

    while $k \leq N$ **or** ($k \neq 1$ **and** $|r_{k-1}^u|_{\max} \leq \xi_u$ **and** $\sum |r_{k-1}^f| \leq \xi_f$) **do**

      Aerodynamic mesh ←displacements u_{k-1} from displacement coupling mesh

      Execute aerodynamic solver ← aerodynamic mesh

      Transfer aerodynamic forces f_k^A to loads mesh f_k

      f_k ← force coupling mesh

      if Use force relaxation **then**

        s_k ← scaling sequence   ▷ User input

        Force coupling mesh ← $f_k = s_k f_k$

      end if

      Structural mesh ← f_k from force coupling mesh

      Execute structural solver ← structural mesh

      Transfer structural displacements u_k^S to displacement coupling mesh u_k

      u_k ← displacement coupling mesh

      if Use displacement relaxation **then**

        t_k ← scaling sequence **or** Aitken   ▷ User input

        Displacement coupling mesh ← $u_k = t_k u_k$

      end if

      $r_k^u ← u_k - u_{k-1}$ ▷ Displacement residual

      $r_k^f ← f_k - f_{k-1}$ ▷ Force residual

      $k = k + 1$

    end while

  end function

For the transfer of the forces and displacements to the different meshes, mediating meshes are used (see section 4.3). Those meshes are used to couple the forces and the displacements between the disciplines. The necessary interpolation or distribution matrices may be based on radial basis functions or nearest neighbours. Which nodal transfer library to be used, which components should be included and which functions to be applied is selected by the user. In this work, a nearest neighbour search is selected for the force transfer and a thin plate spline to interpolate displacement. The aero-structural solver stops if the maximum displacements are below 1 cm and the sum of the force residual is below 500 N. Starting from a jig shape usually leads to higher wing-loads in the outboard region of the wing for backwards swept wings, because the initial elastic twist is zero. Thus, the initial displacements can become too large for the volume mesh deformation. Also, large forces can lead to buckling and structural failure in geometrically nonlinear analyses. Therefore, the user can decide whether to use force relaxation and or displacement relaxation. The scaling of the interpolated forces was inspired by the work of Gray et al in [2]. It allows to dampen the effect of excessively high forces computed in the initial, undeformed shape. Thus, the structure is not loaded beyond failure regime and convergence issues in the updated Lagrangian scheme are minimised.

3.5 Flight mechanic analysis

For the free flying aircraft the six degrees of freedom of the rigid body motion are based on the equations for forces (Eq. 7) and moments (Eq. 8). Forces F and moments L in the body reference frame $_b$ are evaluated at the center of gravity. The mass matrix M and the moment of

inertia tensor $\boldsymbol{J}$ are computed at the center of gravity as well. Further details can be found in work of Waszak et al. [8].

$$M\dot{\boldsymbol{v}}_b = (M\boldsymbol{v}_b) \times \boldsymbol{\Omega}_b + \boldsymbol{F}_b^{aero} + \boldsymbol{F}_b^{ext} + \boldsymbol{F}_b^{grav} \tag{7}$$

$$J\dot{\boldsymbol{\Omega}}_b = (\boldsymbol{J}\boldsymbol{\Omega}_b) \times \boldsymbol{\Omega}_b + \boldsymbol{L}_b^{aero} + \boldsymbol{L}_b^{ext} \tag{8}$$

Note, external forces can be defined like artificial loads to mimic the engine's thrust or an artificial lift distribution for a horizontal tailplane (HTP). The latter principle is used in this work, since the aerodynamic model does not feature an HTP.

As the load factor plays an important role for manoeuvre simulations, it is calculated by the rigid body acceleration, the centrifugal acceleration, and the gravitational acceleration.

$$\tilde{\boldsymbol{n}} = \frac{1}{g}\left(\dot{\boldsymbol{v}}_b - \boldsymbol{\Omega}_b \times \boldsymbol{v}_b + \boldsymbol{g}_b^{\text{grav}}\right) \tag{9}$$

3.6 Trim analysis

The search for a static flight state is implemented as a root finding problem. A target state needs is reached by setting controls which modify parameters like Euler angles, speeds, control surfaces, tailplane rotation, artificial force fields, and more. The Newton based trim solver is detailed in Algorithm 2. A frozen Jacobian can be used, which reduces the computational time as long as the objectives stay roughly linear.

Algorithm 2 The trim solver

Require: Analysis object
  function Execute
      $k = 0$
      $x_0 \leftarrow$ trim controls   ▷ The user specified trim variables
      $\hat{y} \leftarrow$ trim target states   ▷ The user specified trim targets
      $\frac{dr}{dx} = \text{nan}$ **or** $\frac{dr}{dx}_{\text{restart}}$
      while $k \leq N$ **or** $(k \neq 0$ **and** $|r_{k-1}|_{\max} \leq \xi_t)$ **do**
         controls $x_k \rightarrow$ actuators
         Execute analysis
         $y_k \leftarrow$ trim quantities analysis
         $r_k = y_k - \hat{y}$ ▷ Target residual
         if $\frac{dr}{dx} \,! = \text{nan}$ **and** (**not** Use frozen jacobian) **then**
            $\frac{dr}{dx} \leftarrow$ forward finite differencing
         end if
         $\Delta x = -\frac{dr}{dx}^{-1} r_k$ ▷ Newton approach
         if Use relaxation **then**   ▷ User input
            $s_k \leftarrow$ Aitken
            $\Delta x = s_k \Delta x$ in the coupling mesh
         end if
         $x_{k+1} = x_k + \Delta x$
         $k = k + 1$
      end while
  end function

---

4 SIMULATION MODEL

The model used for the presented studies represents a long range jet transport in the category of an Airbus A350 or an Boeing 787. General aircraft characteristics are depicted in Table 1. The

Aircraft Parameter Definitions	
range	15000 km
MTOM	275.0 t
span	65.0 m
length	67.0 m
PAX capacity	332
M_{MO}	0.89
fuel capacity	115.0 t
reference lifting surface area	445.0 m^2
aspect ratio	9.4
leading edge sweep	35.0°
mean aerodynamic chord	9.0 m

Table 1: General aircraft specifications.

simulation model is composed out of three main components: finite element structure, finite volume aerodynamics, and a coupling model for interpolation of displacements and aerodynamic forces. Each component is described in detail below.

4.1 Structural Model

The overall structural model is depicted in Fig. 1a. While the fuselage is represented by a beam, the wing structure is generated using the in-house model generator *ModGen*[9]. The software uses parametric splining to generate enclosed wing surfaces from airfoils and planform parameters. Furthermore, key structural subassemblies, like spars, ribs, and skins, can be freely positioned inside the wing. The output is a discretised fully stiffened shell structure of the aircraft. Additionally, secondary and fuel masses are estimated and attached to the fuselage, engine pylons, and the loads reference axis (*LRA*) at the center of each rib (Fig. 1d). This LRA is connected to the primary wing structure at the intersection of spars, ribs and skins, using RBE3 elements (Fig. 1c). Therefore, the LRA may be used to introduce loads into the structure, integrate cutting loads, or evaluate displacements. The wing is attached to the fuselage by a distributed RBE2 clamping at multiple points of the centre wing box. The loads generation and optimisation of the structure was carried out using a tool-chain build around MSC.Nastran. It's details can found in reference [10]. Using linear aerodynamic and structural methods, various manoeuvre and dynamic gust cases were defined in combination with eight mass cases (Fig. 1b), resulting in over 3000 unique load cases. After an evaluation of the cut loads, those found to be significant are utilised in the structural optimisation. The focus of the optimisation was the primary wing structure.

The optimisation model of the shell elements uses unbalanced lamination parameters in order to describe the anisotropic nature of carbon fibre reinforced plastics (*CFRP*)[11]. Furthermore, the thickness of shell elements and the height of stiffeners were chosen to be design variables. However, the laminate of the stiffeners is kept constant at 70 % 0°, 20 % ±45°, and 10 % 90°. The target function was a composition of primary structural mass and wing tip deflection,

(a) Full structure

(b) Mass cases

(c) Structure, wing box section cut

(d) Exemplary mass distribution, blue: secondary and PAX, red: fuel
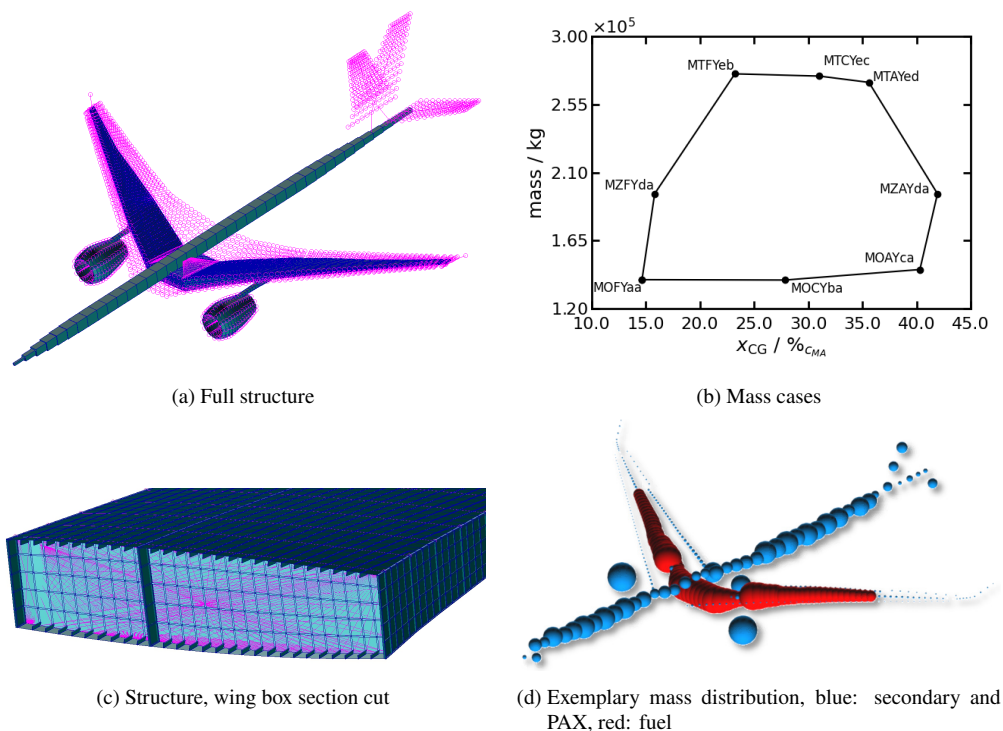
Figure 1: Structural model components

seeking to minimize weight, while increasing flexibility. In order to obtain a flexible yet feasible design, a plethora of constraints were formulated, including, maximal strain, beam crippling, local intracell buckling, global buckling, and compatibility of the lamination parameters after Hammer et al.[12]. Furthermore, by composing a monolithic approach, in which the manoeuvre loads are directly calculated during structural optimisation in Nastran SOL200, it was possible to constrain pitch stability and aileron efficiency as well [10]. Finally, inspired by the work of Gray et al. in [2], the variation in shell thickness and beam height over adjacent design fields were constrained to be less then 10 %. However, this only accounted for connected elements in the same subassembly (e.g. spars). As both, shell thickness and stiffener height, were altered at the same time, this constraint has proven to be effective in order to avoid large discontinuities in properties and smoothing convergence.

As material, IM6 was chosen. It's properties are listed in [13]. However, in order to enlarge the design space and gain overall flexibility, the strain limits were scaled, leading to a maximum allowed tensile strain of 8000 μ. In the context of this paper, the optimisation process is regarded as completed and the focus lies on the evaluation in the context of geometrically nonlinear loads analyses. For further information regarding the model, the employed tool chain, or the optimisation methodologies, please refer to [10], [14], [15].

4.2 CFD Model

Since a three-dimensional geometry of the whole aircraft was not available at present, a simplified CFD-mesh (Fig. 2) is generated based on the outer wing geometry exported by the model generator. The resulting geometry is attached to a symmetry plane and supplemented by a flat wing tip. In order to provide a smooth termination of the wing tip, a cap in the style of a Küchemann-tip is added. Quadrilateral elements are used on the main wing and triangular cells for the symmetry plane and the cap. Furthermore, to efficiently resolve boundary layer effects, layers of hexahedrons and prisms are placed in the vicinity of the surface. In total, the mesh
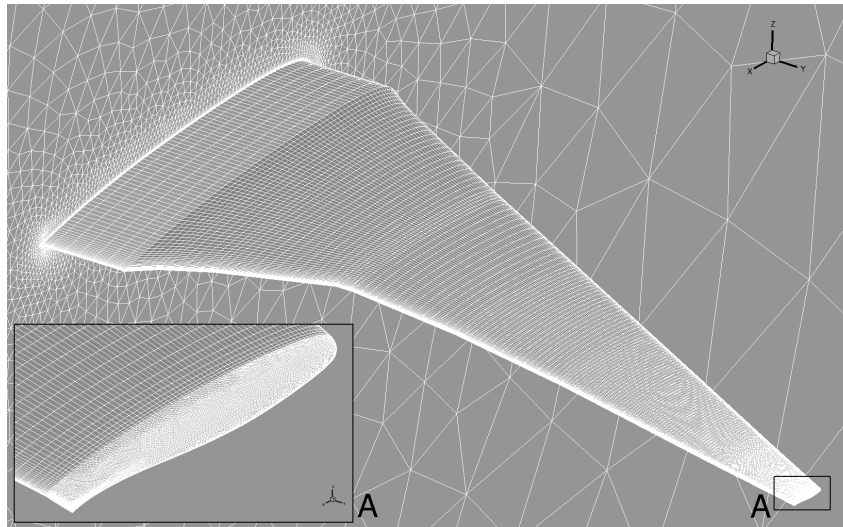
Figure 2: Hybrid CFD mesh. Zoom on wing cap.

consists of 2.6 million nodes and 3.7 million elements.

4.3 Coupling

An intermediate mesh for force and displacement transfer between aerodynamic and structural models is depicted in Fig. 3. Rigid airfoils are extracted from the jig-shape of the CFD-mesh
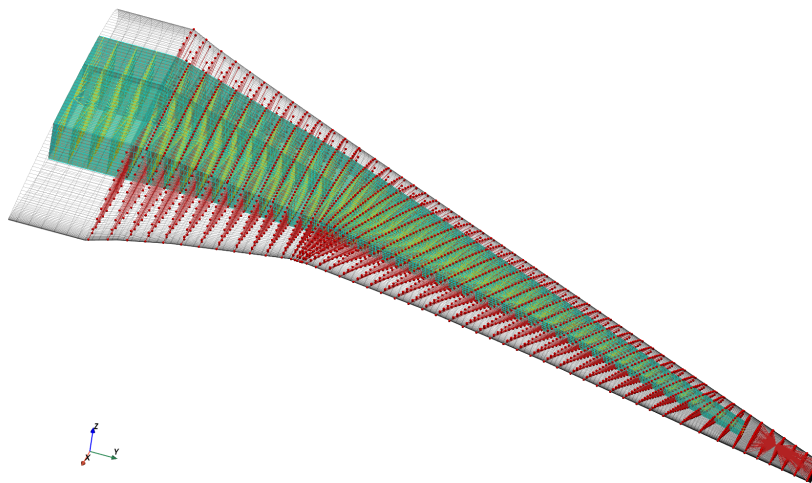

Figure 3: Coupling nodes in red, structural mesh in green, CFD surface mesh in grey, and RBE3 loads reference assembly in yellow

at the position and in the orientation of the wing box ribs. These airfoil are rigidly attached to the loads reference axis at the centre of the wing box. The loads reference axis points on the other hand are attached to the rib-skin-spar intersection by weighted RBE3-elements, as mentioned in Section 4.1. Therefore, the LRA-grids are displaced as a weighted average of the structure, as are the rigidly attached airfoils. Consequently, the displacement of the airfoils can be interpolated onto the aerodynamic mesh. The presented coupling modeling represents a rather traditional approach and will be extended in the future to resolve and transfer changes in camber and skin buckling onto the aerodynamic model.

5 RESULTS

To investigate the effect of considering geometrically nonlinearities, rigid and elastic polars are computed as an initial step. Based on the results of the polar analysis, three trimmed manoeuvres are investigated.

The elastic twist and the bending line shown in the results section are reconstructed by a thin plate spline interpolation based on the structural deformation. The base points are the structural coupling nodes, for which a spline is created, including leading edge, trailing edge, and the 25 % line. Additionaly, the bending component is interpolated at the 25 % line. Lastly, the sectionwise twist is based on the difference of the deformation between leading and trailing edge resolved in the global coordinate system, in which x points in the flow direction and y points to the wing tip.

5.1 Polar Computations

As flight points for quasi-steady manoeuvre simulation are off-design, the simulation of those can become challenging. The flow may become highly non-linear, due to flow separations, compression shocks, interaction between shocks, and flow separation. Also, the steady flow assumption may be invalid when those effects start to occur. A simple polar analysis with respect to the angle of attack allows a first evaluation which problems may become dominant and in what range the discretised physical model can be trusted.

The polar computation is conducted for multiple angles of attack (AoA) in steps of $0.5°$ from $−0.5°$ to $9°$. Furthermore, the polar analysis is performed for a rigid aerodynamic analysis, an aerodynamic analysis coupled with a linear-elastic structural analysis, and an aerodynamic analysis coupled with a geometrically nonlinear structural analysis. The selected altitude is $4777\,\text{m}$ at a Mach number of 0.67.

The resulting lift coefficient with respect to the angle of attack is shown in Fig. 4. The rigid analysis computes larger lift coefficients for the same angle of attack at a steeper slope compared to the elastic analyses. Compared to the linear structural analysis, the geometrically nonlinear analysis computes smaller lift coefficients. The deviation starts at about $3°$ at a lift coefficient of 0.5. The plateau for the maximum lift coefficient can be seen for all three types of analyses and
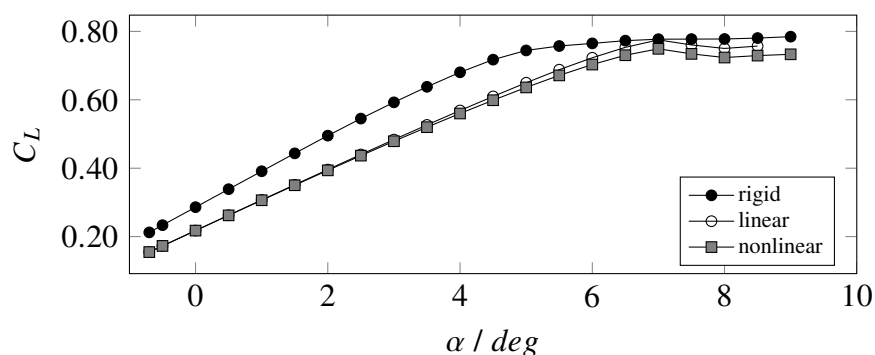

Figure 4: Lift coefficient with respect to the angle of attack.

it is related to flow separation. To quantify the separation of the flow, the percentage of surface nodes with a negative skin friction is calculated. Wingtip and the blunt trailing edge are excluded from the latter calculation. Figure 5 visualises the percentage of nodes with separation. Flow separation is predicted for all simulations at larger angles of attack and the flow separation pattern
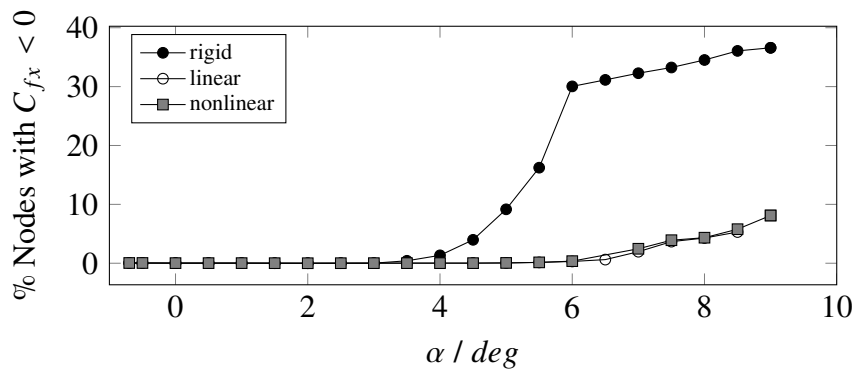
Figure 5: Percentage of surface nodes with a negative skin friction coefficient. Nodes of the trailing edge and the wingtip are excluded.

for the linear and the nonlinear analysis seems to be similar as their difference is negligible. For angels of attack above 5.5°, more than 30 % of the surface nodes are in regions with negative skin friction for the rigid computation. Different regions of reversed flow are visualised in Fig. 6. A strong pressure gradient close to the leading edge was observed to be the main cause for the
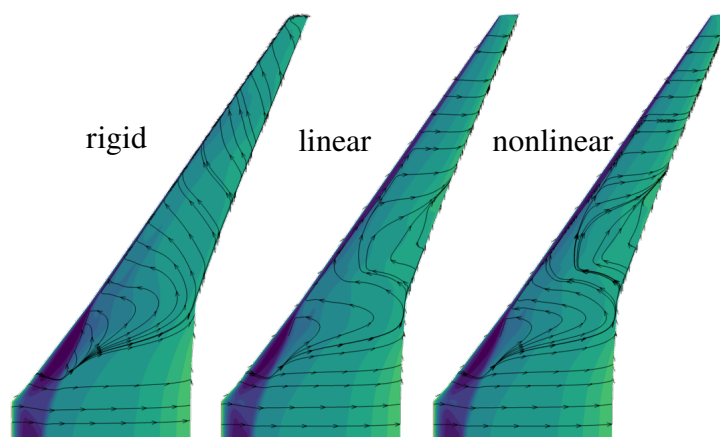
Figure 6: Pressure coefficient at $\alpha = 8°$, for a rigid, linear and geometric nonlinear analysis, static coupling, plotted on jig-shape.

flow separation. While the complete outer part of the flow is detached for the rigid analysis, only a larger region about the position of the kink shows flow separation for the elastic analyses. It has to be pointed out, that the flow solution with large regions of separated flow may not be valid. At least the steady flow assumption, the choice of the SA-Neg turbulence model and the mesh density should be taken with caution. The differences between rigid and elastic simulation can be explained by the reduction of the local angles of attack due to the elastic twist. For the linear elastic and the nonlinear elastic analysis, the wing twist reduces the local AoA, which reduces the lift and shifts the flow separation to higher angles of attack. Due to the different local angle of attack, the separated flow regions in Fig. 6 differ strongly between the rigid and the elastic analyses. While for the rigid analysis the complete outer region of the wing is separated, the elastic analysis exhibits detached flow in the region of the kink. The wing tip twists about $-4°$ for the nonlinear and $-5°$ for the linear analysis as shown in Fig. 7. As the elastic twist for the linear case is stronger, it is expected that less lift is generated. However, the opposite is observed. This can be explained when looking at the bending line over the normalized spanwise
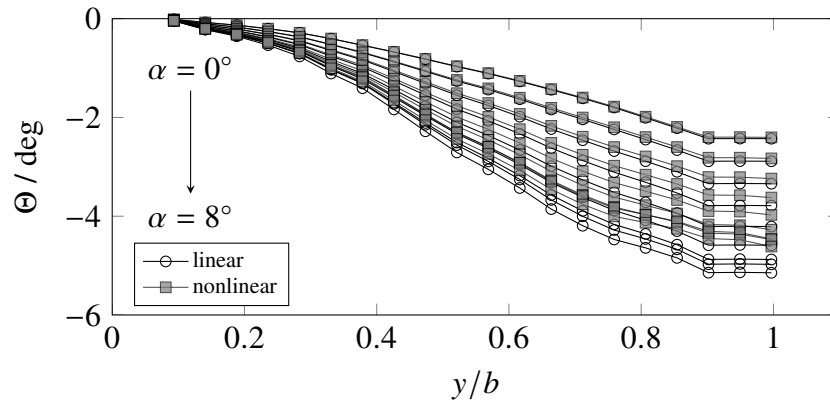
Figure 7: Twist over spanwise position normalised by deformed half span, $\alpha \epsilon\,[0, 8]$, 1° steps.

position in Fig. 8. Here, the geometric nonlinearity of the flexible wing becomes apparent.
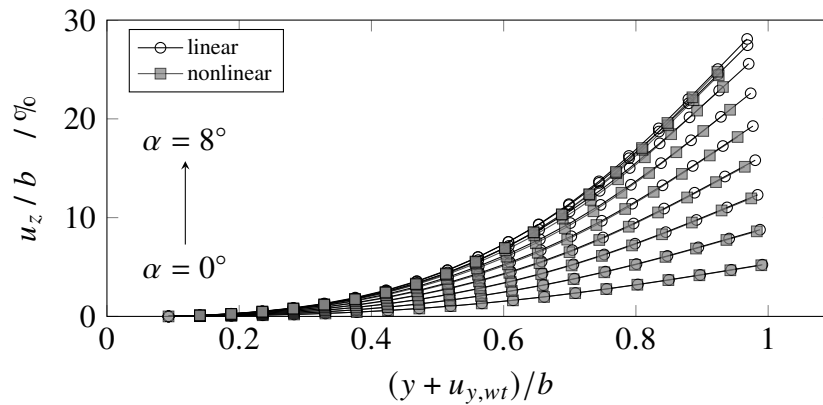

Figure 8: Bending line over spanwise position normalised by undeformed half span, $\alpha \epsilon\,[0, 8]$, 1° steps.

The nonlinear analysis reaches deformations of about 26 % while the linear analysis estimates 29 %. Furthermore, the linear analysis elongates the wing and shows a smaller curvature. The elongation of the wing leads to an increase of the wetted surface area, which increases the lift. The increased lifting area over the tip deflection is shown in Fig. 9. The geometrically linear
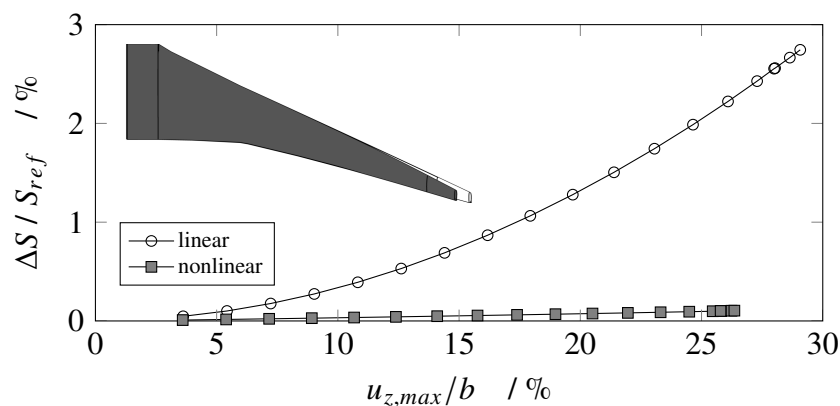
Figure 9: Relative change in lifting surface due to deformation - right wing.

analysis of the highly loaded wing, yields a 2.5% larger lifting area, which relates well to the observed difference in the lift coefficient. Since the lifting area is increased towards the wing

13

tip, the additional lift is generated outboard. As a consequence, the bending moment in Fig. 10 of the linear analysis is larger compared to bending moment of the nonlinear analysis. Larger
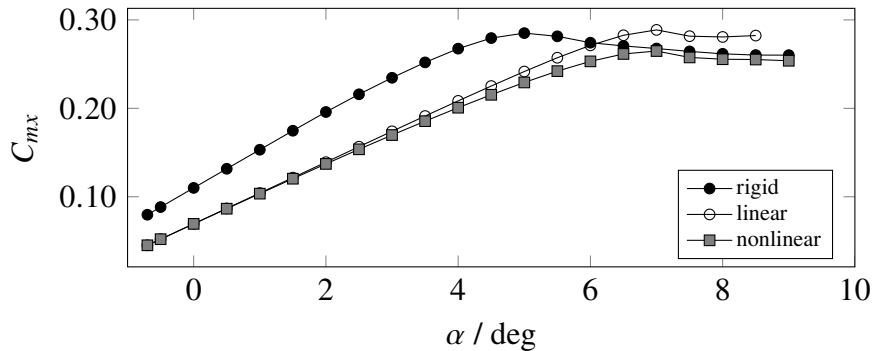

Figure 10: Aerodynamic bending moment coefficient with respect to the angle of attack for the half wing.

differences are observed for the pitching moment coefficient for all polars in Fig. 11. The strong
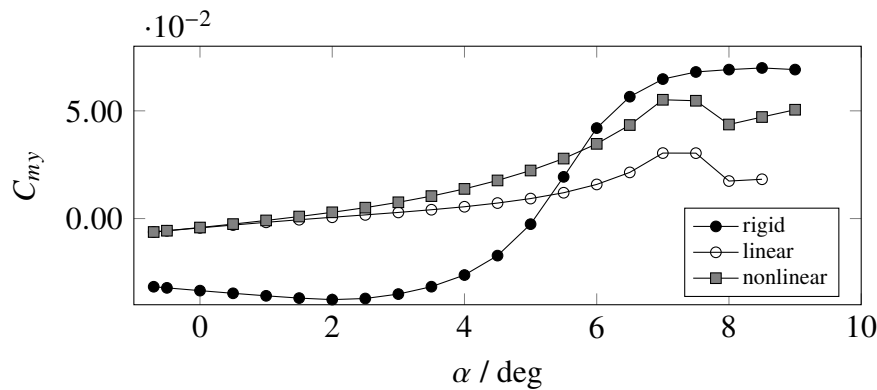

Figure 11: Aerodynamic pitching moment coefficient with respect to the angle of attack.

change of the pitching moment calculated by the rigid analysis for the different angles of attack can be explained by the flow separation. The pitching moment of the nonlinear analysis is larger than the pitching moment of the linear analysis and both show a positive gradient with respect to the angle of attack. With the increased surface at the wing tip from the linear analysis, the contribution to the negative torsion moment is larger as well. This results in larger pitching moments for the nonlinear analysis at this flight point.

A summary of the most important aerodynamic quantities is given in Table 2. The derivatives with respect to the angle of attack are based on a linear regression for angle of attacks from $0°$ to $3.5°$.

Elasticity	$C_{L,w,\max}$	$dC_{L,w}/d\alpha$	$dC_{my,w}/d\alpha$	$\dfrac{dC_{my,w}/d\alpha}{dC_{L,w}/d\alpha}$
Rigid	0.794	5.857	-0.0764	-0.0130
Linear	0.751	5.082	0.1406	0.0277
Nonlinear	0.749	4.998	0.2207	0.0442

Table 2: Characteristic aerodynamic quantities for the polar analysis.

5.2 Trimmed manoeuvres

In the following, trimmed manoeuvres are analysed in order to compare geometrically linear and nonlinear simulations of the same flight state. As depicted in Table 3, three states are defined, including a level cruise flight, a -1.0 g push down, and a 2.5 g pull up manoeuvre. Based on the the polar simulations it is clear that the required lift for a 2.5 g manoeuvre at an altitude of 4777.0 m cannot be generated with the current configuration. Since the largest load factor of a given configuration and trim state is defined by

$$n_{Z,\max} = C_{L,\max} \frac{q_0 S_{\text{ref}}}{mg},\qquad(10)$$

the manoeuvre calculations are executed a sea level, avoiding the stall region and simplifying the methodical comparison. The pull up manoeuvre is conducted at dive speed, whereas the speed of the push down is reduced to maximum operating speed in accordance with European certification specifications [16]. The manoeuvres are trimmed by specifying a constant pitch rate $q(n_Z)$, while the free trim variables are the angle of attack and a point force at the position of the HTP. Targets are the load factor and a pitching acceleration of zero. As the results depicted in

CSM	Alt. / m	Mach	n_Z	q / $^{rad}/_s$	α / deg	$C_{mx,w}$	$C_{my,w}$	$C_{L,w}$	u_z, wt / m
Lin.	0.0	0.51	-1.0	-0.112	-6.57	-0.131	-0.0371	-0.328	-3.70
NL	0.0	0.51	-1.0	-0.112	-6.60	-0.130	-0.0386	-0.328	-3.64
Lin.	10668.0	0.85	1.0	0.0	2.04	0.205	-0.0378	0.539	3.86
NL	10668.0	0.85	1.0	0.0	2.06	0.203	-0.0343	0.538	3.77
Lin.	0.0	0.57	2.5	0.0762	6.03	0.256	0.0149	0.695	8.01
NL	0.0	0.57	2.5	0.0762	6.18	0.245	0.0318	0.689	7.60

Table 3: Trim manoeuvre specifications and results.

Table 3 show, the differences in the cruise and push down cases between the geometrically linear and nonlinear calculations are rather marginal. The nonlinear calculations require a slightly larger angle of attack while resulting in a smaller vertical tip displacement $u_{z,wt}$. However, these differences amplify for the pull up manoeuvre. Furthermore, as already seen for the polar computations, $C_{my,w}$ reaches over two times the value as the linear counterpart for the latter manoeuvre, caused by a different bending-twist coupling and retention of the wing's lifting surface. These findings are backed by the bending and twist lines, plotted over the normalised half span in Fig. 12 and Fig. 13 respectively. Bending and twist of the cruise and push down cases are very similar. The results only reveal a small stretch in the linear models compared to the nonlinear, while the curvature is nearly identical. Furthermore, the twist of the nonlinear model is only slightly smaller. Again these differences increase significantly for the pull up manoeuvre, as the stretching of the wing becomes more dominant. Additionally, the curvature of the nonlinear calculation is overall higher. This is accompanied by significantly larger torsion of the wing. Thus, the local lift of the nonlinear calculation is larger further outboard of the wing. This potentially goes along with a stiffness reduction due to the force-displacement adaptive formulation in the Lagrangian method, causing the higher curvature of the bending. In combination with the sweep of the wing, this might also be the reason for the noticeably larger C_{my}, as the portion of the lift distribution is shifted further down stream. To complement these findings, Fig. 14 and Fig. 15 depict the cutting loads of the bending and torsion moment, respectively. Due to limitations of MSC.Nastran, the applied aerodynamic and inertia loads are
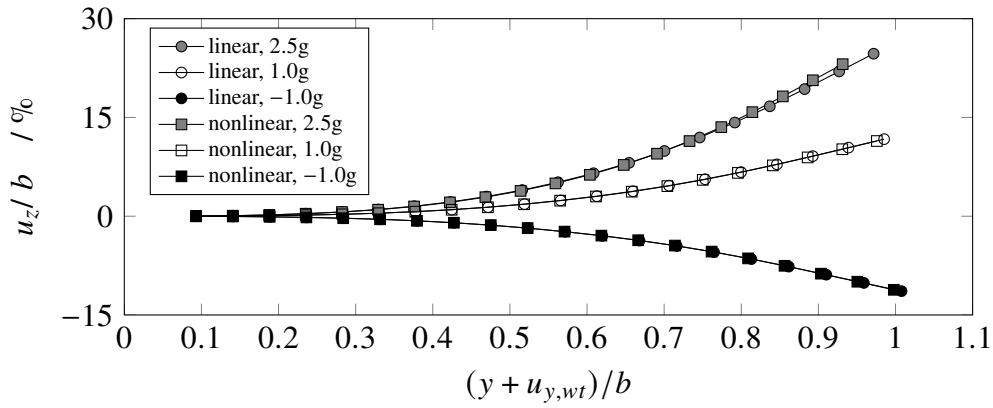
Figure 12: Bending deformation over spanwise position normalised by reference half span.
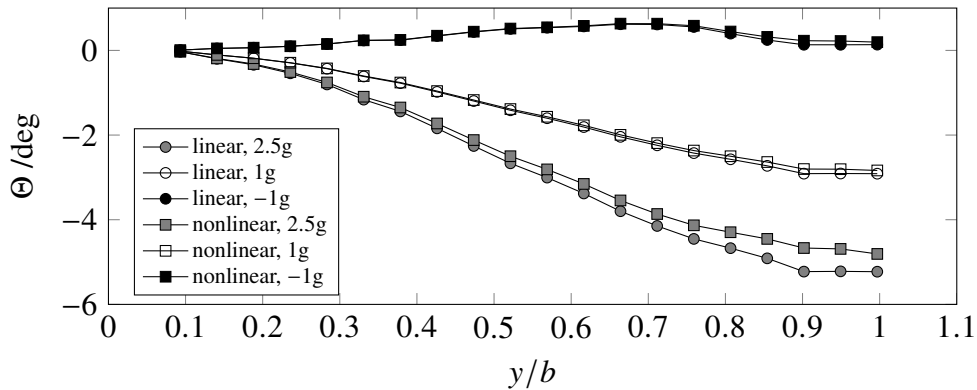

Figure 13: Twist deformation over spanwise position normalized by deformed half span.
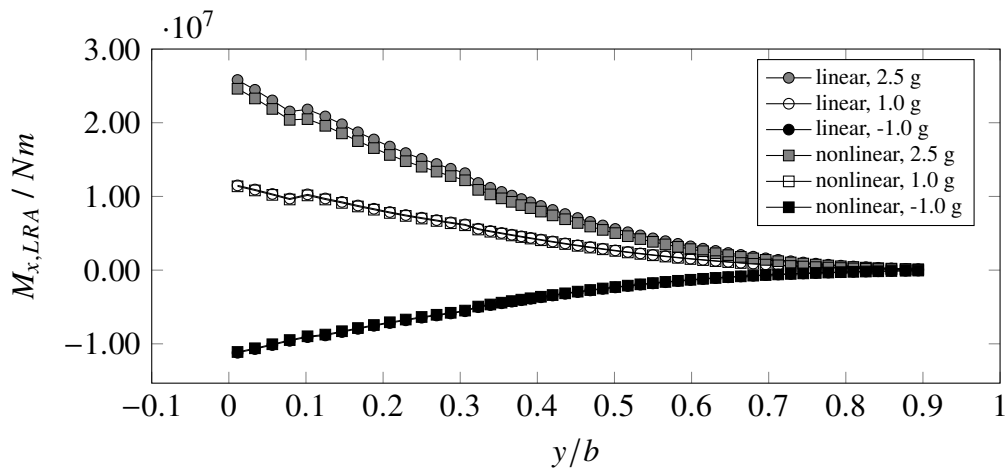

Figure 14: Bending moment over spanwise position normalised by reference half span, loads reference axis coordinate system.

summed on the jig-shape rather than in the deformed state. Furthermore, the cutting loads are plotted in the coordinate system of the loads reference axis, in which the x-axis points to the trailing edge and the y-axis runs in the centre between the spars. This results in several jumps in the integrated loads. The fist jump occurs at the transition of centre and outer wingbox at $\eta \simeq 0.08$, as the sweep changes from 0° to approximately 35°. Furthermore, several degrees of freedom at this position are attached to the clamping, reducing the meaningfulness of the inboard loads. The second discontinuity appears at $\eta = 0.3$. This is approximately the position
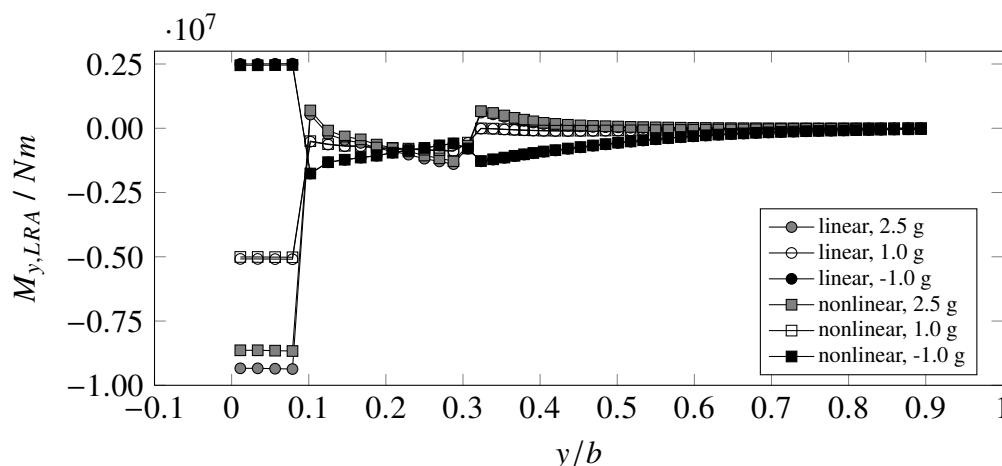
16

Figure 15: Torsion moment over spanwise position normalised by reference half span, loads reference axis coordinate system.

of the engine and the kink. Not only does this result in a rotation of the output coordinate system, but the included mass of the engine introduces large concentrated loads. In combination with the missing aerodynamic representation of the engine, this results in a rather unusual trend of the cutting loads for $\eta \leq 0.3$. Nevertheless, the cutting loads trends allow for a qualitative comparison of the geometrically linear and nonlinear simulations.

Once more, the deviation in bending and torsion moments for the cruise and push down cases are negligible. Therefore, the increase in computational cost from one minute for the linear calculation, to fifteen minutes for the nonlinear variant, cannot be justified. However, as seen for the displacements, the differences between linear and nonlinear calculations rise drastically for the 2.5 g pull up manoeuvre. The wing bending moment of the linear computation is overall higher than the nonlinear counterpart, up to a difference of 4.8 % at the wing root. This effect is mainly caused by the increase in lifting surface in the linear calculation, albeit the loads integration of the wing is carried out on the jig shape. A cutting moment calculation on the deformed mesh might even increase this effect. In any case, the increase in the linear calculation exceeds any rise in bending moment caused by the less negative wing torsion in the nonlinear calculation. The wing torsion moment outside of the centre wing box is overall slightly higher for the nonlinear calculation, which again corresponds to the less negative wing torsion.

Since the torsion moments are one magnitude smaller than the bending moments, one would naturally assume the linear calculations to be conservative with respect to failure indices. However, the latter assumption is invalidated by the evaluation of the von Mises strain in Fig. 16. These illustrations depict the difference in von Mises strain of plate elements of the geometrically nonlinear calculation with respect to the linear counterpart. In the context of the -1.0 g push down manoeuvre the deviation is rather small and with a peak of -200 μ the linear calculation is found to be indeed conservative. On the other hand, for the 2.5 g pull up the difference rises to a massive value of up to 2000 μ on the outer section of the wing. This position corresponds with the increased curvature in the bending line and the smaller degree in torsion. Consequently, the differential stiffness formulation in the nonlinear Lagrangian method results in a reduction in bending stiffness, ultimately leading to higher strain values. Thus, in order to accurately evaluate strain based failure indices for large deflections, geometrically nonlinear calculations become inevitable.

(a) -1.0 g pull up manoeuvre.
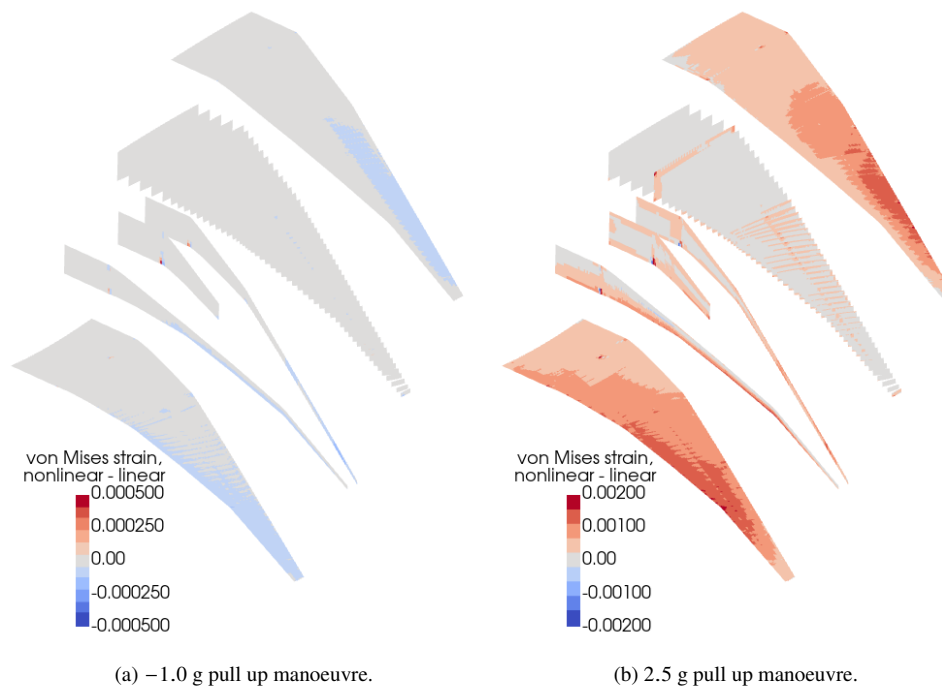
(b) 2.5 g pull up manoeuvre.

Figure 16: Difference in von Mises strain, nonlinear - linear

In order to properly evaluate the impact on structural optimisation, further investigations have to be conducted. Therefore, a more detailed evaluation of principle strains of multiple element types, global buckling analyses based on differential stiffness in the deformed state, and an analysis of beam crippling are planned as a subjects for future publications.

6 CONCLUSION

By coupling high fidelity CFD analyses with geometrically linear and nonlinear structural methods, this paper analysed the impact of large wing deflections on the loads calculations process. For this purpose a highly flexible structural model of a long range jet transport, optimised by means of linear methods, has been paired with a nonlinear aerodynamic model. In this paper, the methodology to compute coupled polars and trimmed, quasi-steady manoeuvres has been presented.

In case of the polar computations, rigid analyses showed poor agreement with the flexible counter parts. The overall lift coefficient and it's gradient is overestimated. Furthermore, the maximal lift is higher than in the flexible computations and the flow detachment starts at smaller angle of attack. On the other hand, the linear and nonlinear flexible calculations show good agreement in the development of detached flows. Nevertheless, the linear computations are capable of reaching higher maximal lift coefficients before stalling completely. The most significant differences come down to the nonlinear calculations retaining the overall lifting surfaces well. The linear calculation on the other hand stretches the reference area for large deflections by up to 2.7 %. In combinations with the differential stiffness in the nonlinear calculation, this results in a different twist-bending coupling, in which the nonlinear calculation results in a significantly less negative torsion for large deflections than the linear counterpart. This is accompanied by noticeably higher pitching moment coefficient of the wing ($C_{my,w}$). Furthermore, the lift coefficient for the same angle of attack are higher for the linear calculations. This is influenced by the increase in lifting area, since the deviation becomes predominant for larger angles of attack.

These characteristics are also valid in the context of the static manoeuvre calculations. Trimming the aircraft to the same state allowed for a direct comparison of linear and nonlinear loads. In terms of the cruise flight and push down manoeuvres, the differences are negligible. The deviations in strech, bending, torsion, cut loads, and strain do not justify the increase in simulation time by a factor of over fifteen of a nonlinear calculation. However, for the 2.5 g pull up manoeuvre the differences increase drastically. As a result of the nonlinear calculation the bending deformation along the wing is steeper at the outer section. Furthermore, the twist remains overall less negative, resulting in more lift being generated at the outer portion of the wing. Due to the increase in lifting surface area, the required angle of attack for the linear calculation is smaller. The effect on the pitch moment coefficient which emerged in the polar computations also appears for the trim calculations, with the nonlinear calculation resulting in a coefficient twice as high as for the linear simulation. Potentially as a result of the wing stretching, the bending moment of the linear calculation is overall higher. Interestingly, the comparison of the von Mises strain reveals significantly higher values for the nonlinear calculation which underlines the higher curvature in the bending line. Thus, despite the higher bending moment and the increased lifting area of the linear calculation, the latter cannot be regarded as conservative, highlighting the need for geometrically nonlinear calculations to accurately evaluate strain based failure indices.

Based on the presented work, several task have been identified for future research. First of all, the coupling model will be updated to enable the transfer of buckling effects and changes in camber onto the aerodynamic mesh. Secondly the dynamic simulation of gust encounters with nonlinear deflections is required to fulfill certification specifications. Furthermore, the initial investigation of the failure indices will be extended to include criteria like buckling and crippling. Lastly, the dependency of modal characteristics on the structural displacements and the differential stiffness is subject of interest.

REFERENCES

[1]   M. Ritter and C. E. S. Cesnik, "Large Deformation Modeling of a Beam Type Structure and a 3D Wingbox using an Enhanced Modal Approach," in *57. AIAA/ASCE/AHS/ASC Structures, Structural Dynamics, and Materials Conference*, San Diego, Jan. 2016.

[2]   A. C. Gray and J. R. R. A. Martins, "Geometrically Nonlinear High-fidelity Aerostructural Optimization for Highly Flexible Wings," in *AIAA SciTech Forum*, Virtual Event, Jan. 2021.

[3]   D. Schwamborn, T. Gerhold, and R. Heinrich, "The DLR TAU-code: Recent applications in research and industry," in *ECCOMAS CFD 2006: Proceedings of the European Conference on Computational Fluid Dynamics, Egmond aan Zee*, Egmond aan Zee, The Netherlands, Sep. 2006.

[4]   L. Reimer, R. Heinrich, S. Geisbauer, *et al.*, "Virtual aircraft technology integration platform: Ingredients for multidisciplinary simulation and virtual flight testing," in *AIAA SciTech Forum*, Virtual Event, Jan. 2021. [Online]. Available: `https://elib.dlr.de/140244/`.

[5]   J. M. Feldwisch and M. Schulze, "High-fidelity aeroelastic loads calculation for a transport aircraft configuration including pitch and roll maneuvers," in *Notes on Numerical Fluid Mechanics and Multidisciplinary Design*, Springer International Publishing, 2021, pp. 527–536. [Online]. Available: `https://doi.org/10.1007/978-3-030-79561-0_50`.

[6] J. Feldwisch, L. Reimer, and M. Ritter, "UltraFLoads – A Framework for High-Fidelty Loads Computations," in *70. German Aerospace Congress*, Bremen - Digital Event, Aug. 2021.

[7] *MSC Nastran 2021 Nonlinear User's Guide*, MSC.Software, Nov. 2020, pp. 117–158.

[8] M. R. Waszak, C. S. Buttrill, and D. K. Schmidt, "Modeling and model simplification of aeroelastic vehicles: An overview," NASA Langely Research Center, Tech. Rep. NASA TM-107691, 1992.

[9] T. Klimmek, "Static Aeroelastic Requirements in Multidisciplinary Structural Design of Jet Transport (original: Statische aeroelastische Anforderungen beim multidisziplinären Strukturentwurf von Transportflugzeugflügeln)," Original document in German, Ph.D. dissertation, Technische Universität Braunschweig, Germany, 2016. [Online]. Available: http://elib.dlr.de/105799.

[10] M. Zimmer, "Integral Design and Optimisation Process for a Highly Flexible Generic Long Range Jet Transport with Flight Mechanic Derivative Constraints," Virtual Event, Jan. 2021.

[11] S. W. Tsai and N. J. Pagano, "Invariant Properties of Composite Materials," Defense Technical Information Center, Tech. Rep. AD0668761, Mar. 1968.

[12] V. Hammer, M. Bendsøe, R. Lipton, and P. Pedersen, "Parametrization in laminate design for optimal compliance," *International Journal of Solids and Structures*, vol. 34, pp. 415–434, 4 Feb. 1997.

[13] I. M. Daniel and O. Ishai, "Engineering Mechanics of Composite Material," Oxford Universiy Press In., Oxford, Tech. Rep., 1994.

[14] M. Zimmer and K. Bramsiepe, "Design and Optimisation of a Highly Flexible Wing Structure for a Generic Long-range Aircraft," in *68. German Aerospace Congress*, Darmstadt, Sep. 2019.

[15] M. Zimmer and V. Handojo, "Impact of Gust Loads and Manoeuvre Load Alleviation Techniques on the Design of a Highly Flexible Jet Transport," in *69. German Aerospace Conference*, Aachen - Virtual Event, Sep. 2020.

[16] European Aviation Safety Agency, *Certification Specifications and Acceptable Means of Compliance for Large Aeroplanes, CS-25*. 2019, Amendment 23, Subpart B and C. [Online]. Available: https://www.easa.europa.eu/document-library/certification-specifications/cs-25-amendment-25.

COPYRIGHT STATEMENT